

Reconstruction of the CMB lensing for Planck

L. Perotto^{1,2}, J. Bobin^{3,4}, S. Plaszczynski², J.-L. Starck³, and A. Lavabre²

¹ Laboratoire de Physique Subatomique et de Cosmologie (LPSC), CNRS : UMR5821, IN2P3, Université Joseph Fourier - Grenoble I, Institut Polytechnique de Grenoble, France

e-mail: perotto@lpsc.in2p3.fr

² Laboratoire de l'Accélérateur Linéaire (LAL), CNRS : UMR8607, IN2P3, Université Paris-Sud, Orsay, France

e-mail: plaszczy@lal.in2p3.fr, lavabre@lal.in2p3.fr

³ Laboratoire AIM (UMR 7158), CEA/DSM-CNRS-Université Paris Diderot, IRFU, SEDI-SAP, Service d'Astrophysique, Centre de Saclay, F-91191 Gif-Sur-Yvette cedex, France

e-mail: jstarck@cea.fr

⁴ Applied and Computational Mathematics (ACM), California Institute of Technology, 1200 E. California Blvd, M/C 217-50, PASADENA CA-91125, USA

e-mail: bobin@acm.caltech.edu

Received November 12, 2009

ABSTRACT

Aims. We prepare real-life Cosmic Microwave Background (CMB) lensing extraction with the forthcoming Planck satellite data, by studying two systematic effects related to the foregrounds contamination: the impact of foreground residuals after a component separation on the lensed CMB map, and of removing a large contaminated region of the sky.

Methods. We first use the Generalized Morphological Component Analysis (GMCA) method to perform a component separation within a simplified framework which allows a high statistics Monte-Carlo study. For the second systematic, we apply a realistic mask on the temperature maps and then, restore them using a recent inpainting technique on the sphere. We investigate the reconstruction of the CMB lensing from the resultant maps using a quadratic estimator in the flat sky limit and on the full sphere.

Results. We find that the foreground residuals from the GMCA method does not alter significantly the lensed signal, nor does the mask corrected with the inpainting method, even in the presence of point sources residuals.

Key words. Cosmic microwave background – Gravitational lensing – Large-scale structure of Universe – Methods: statistical

1. Introduction

Cosmic Microwave Background (CMB) temperature anisotropies and polarisation measurements have been one of the key cosmological probes to establish the current cosmological constant Λ and Cold Dark Matter (Λ CDM) paradigm. Reaching the most precise measurement of these observables is the main scientific goal of the forthcoming or on-going CMB experiments – such as the *European Spacial Agency* satellite PLANCK¹ which has been successfully launched on the 14th of May 2009 and has currently begun collecting data.

PLANCK is designed to deliver full-sky coverage, low-level noise, high resolution temperature and polarisations maps (see Tauber 2006; The Planck Consortia 2005). With such high quality observations, it becomes doable to extract from the CMB maps cosmological informations beyond the angular power spectra (two-points correlations, hereafter APS), by exploiting the measurable non-Gaussianities (see e. g. Komatsu (2002); The Planck Consortia (2005)).

The weak gravitational lensing is one of the sources of non-Gaussianity affecting the CMB after the recombination (see Lewis & Challinor (2006) for a review). The CMB photons are weakly deflected by the gravitational potential of the intervening large-scale structures (LSS), which perturbs the Gaussian statistic of the CMB anisotropies (Bernardeau

1997; Zaldarriaga 2000). Conversely, it becomes possible to reconstruct the underlying gravitational potential by exploiting the higher-order correlations induced by the weak lensing in the CMB maps (Bernardeau 1997; Guzik et al. 2000; Takada & Futamase 2001; Hu 2001b; Hirata & Seljak 2003a).

The relevance of the CMB lensing reconstruction for the Cosmology is twofold. First, for the sake of measuring the primordial B-mode of polarisation predicted by the inflationary models (Kamionkowski et al. 1997; Seljak & Zaldarriaga 1997), the CMB lensing is a major contaminant. It induces a secondary B-mode polarisation signal in perturbing the E-mode polarisation pattern (Zaldarriaga & Seljak 1998). A lensing reconstruction allowing the *delensing* of the CMB maps is required to recover the primordial B mode signal (Knox & Song 2002; Seljak & Hirata 2004). However, CMB lensing is also a powerful cosmological probe of the matter distribution integrated from the last scattering surface to us. In a near future, it is an unique opportunity to probe the full-sky LSS distribution, with a maximum efficiency at redshift around 3, where structures still experience a well described linear growth (Lewis & Challinor 2006). A lensing reconstruction would largely improve the sensitivity of the CMB experiments to the cosmological parameter affecting the growth of the LSS, such as neutrino mass or dark energy (Hu 2002; Kaplinghat et al. 2003; Lesgourgues et al. 2006; Perotto et al. 2006).

Although well-known theoretically (Blanchard & Schneider 1987), the CMB lensing has never been directly measured. Smith et al. (2007) and Hirata et al. (2008) have found evidence

¹ <http://www.rssd.esa.int/index.php?project=PLANCK&page=index>

for a detection of the CMB lensing in the WMAP data by correlating with several other LSS probes (Luminous Red Galaxies, Quasars and radio sources) at 3.4σ and 2.5σ level respectively. This situation is expected to change with the forthcoming PLANCK data. PLANCK will be the first CMB experiment allowing to measure the underlying gravitational potential without requiring any external data. However, even with the never before met quality of the PLANCK data, CMB lensing reconstruction will be challenging. CMB lensing is a very subtle secondary effect, affecting the smaller angular scale at the limit of the PLANCK resolution in a correlated way over several degrees on the sky. As already quoted, CMB lensing reconstruction is based on the induced non-Gaussianities in the CMB maps, in the form of mode coupling. Consequently, any process resulting in coupling different Fourier moments is a challenging systematic to deal with in order to retrieve the lensing signal (see Su & Yadav (2009) for a recent study of the impact of instrumental systematics on the CMB lensing reconstruction bias). Astrophysical components and other secondary effects might also be a source of non-Gaussianity. These components include : Thermal and Kinetic Sunyaev-Zel'dovich effects (tSZ and kSZ), due to the scattering of CMB radiation by electrons within the galaxy clusters (Sunyaev & Zeldovich 1970); foreground emissions, such as synchrotron, Bremsstrahlung and dust diffuse galactic emission as well as extragalactic point sources. All these components may give a sizable contribution to the level of non-Gaussianities in the CMB maps (Aghanim & Forni 1999; Argüeso et al. 2003; Amblard et al. 2004; Riquelme & Spergel 2007; Babich & Pierpaoli 2008).

The impact of most of the aforementioned effects on the CMB lensing analysis with WMAP data has been investigated by Hirata et al. (2008). The fact that they found a negligible contamination level is encouraging. However, such a result could change when one considers the higher resolution, better sensitivity maps provided by PLANCK. In Barreiro et al. (2006), the component separation impact on non-Gaussianity was studied in the framework of the PLANCK project, but no lensing reconstruction was performed. Hence, the impact of these foreground residuals on the CMB lensing reconstruction is still to be studied.

The overall purpose of the present study is to give an insight to the issues we should deal with before undertaking any complete study of the CMB lensing retrieval with PLANCK: what is the impact of the foreground residuals on the CMB lensing reconstruction? Will it still be possible to reconstruct the CMB lensing after a component separation process or will such a process alter the temperature map statistics? How should we deal with the masking issue? Beyond the *detection* of the CMB lensing signal, we tackled the *reconstruction* of the underlying projected potential APS. We investigated two issues, the impact of a component separation algorithm on the lensing reconstruction and the impact of a masked temperature map restoration before applying a deflection estimator.

Sect. 2 briefly review the CMB lensing effect and the reconstruction method. We present in Sect. 3 an analysis of the impact of one component separation technique, named *Generalized Morphological Component Analysis* (GMCA) (Bobin et al. 2008), which is one of the different methods investigated by the PLANCK consortium (Leach et al. 2008). In Sect. 4, we show how a recent gap filling method (i.e. inpainting process) (Abrial et al. 2008) may solve the masking problem, which may be one of the major issue for the CMB lensing retrieval since it introduces some misleading correlations between different angular scales in the maps.

2. CMB lensing

In this section, we briefly review the CMB lensing effect and the reconstruction method. We introduce the notations used throughout this paper.

CMB photons geodesic is weakly deflected by the gravitational potential from the last scattering surface to us. Observationally, this effect results in a remapping of the CMB temperature anisotropies $T = \Delta\Theta/\Theta_{\text{CMB}}$, according to Blanchard & Schneider (1987):

$$\widetilde{T}(\hat{n}) = T(\hat{n} + \mathbf{d}(\hat{n})). \quad (1)$$

In words, the lensed temperature \widetilde{T} in a given direction of the sky \hat{n} is the temperature T one would have seen in the neighboring direction $\hat{n} + \mathbf{d}(\hat{n})$ in the absence of any intervening mass. The deflection angle, $\mathbf{d}(\hat{n})$, is the gradient of the line-of-sight projection of the gravitational potential², $\mathbf{d}(\hat{n}) = \nabla\phi(\hat{n})$, where ϕ can be calculated within the Born approximation, as the integral along the line-of-sight of the tridimensional gravitational potential (Challinor & Lewis 2005).

The CMB lensing probes the intervening mass in a broad range of redshifts, from $z_* = 1090$, at the last scattering surface, to $z = 0$, with a maximum efficiency at $z \sim 3$. At such a high redshift, the LSS responsible for the CMB lensing (with typical scale of $300h^{-1}Mpc$) still experience a linear regime of growth. As a result, the projected potential ϕ can be assumed to be a Gaussian random field; The consequences of the non-linear corrections to ϕ are shown to be weak on the CMB lensed observables (Challinor & Lewis 2005). Thus, this hypothesis holds very well as long as the CMB lensing study doesn't aim at measuring a correlation with other LSS probes at lower redshifts.

Besides, in the standard Λ CDM model, the deflection angles have a rms of ≈ 2.7 arcmin and can be correlated over several degrees on the sky. The typical scales of the lensing effects are small enough for a convenient analysis within the flat sky approximation. The projected potential may be decomposed on a Fourier basis $\phi(\mathbf{k})$, and its statistics is completely defined by:

$$\langle \phi(\mathbf{k}_1)\phi(\mathbf{k}_2) \rangle = (2\pi)^2 \delta(\mathbf{k}_1 + \mathbf{k}_2) C_{k_1}^{\phi\phi}, \quad (2)$$

where $C_{k_1}^{\phi\phi}$ is the full-sky projected potential APS taken at a multipole $l = |\mathbf{k}_1|$ and it is related to the deflection APS by :

$$C_k^{\text{dd}} = k^2 C_k^{\phi\phi} \quad (3)$$

The lensed CMB temperature APS can be derived from the Fourier transform of Eq. (1) (e. g. as in Okamoto & Hu (2003)). Lensing effect slightly modifies the APS of the CMB temperature, weakly smoothing the power at all angular scale at the benefit of the smaller angular scales. Deeply in the damping tail, at multipole $l \gtrsim 3000$, lensing contribution even dominates over the pure CMB one. However, the main observational consequences of the CMB lensing effect lies beyond the APS. The remapping induces non-Gaussianities in the CMB temperature field, in the form of some correlations between different angular scales.

Consequently, the two-point correlation function of the lensed temperature modes, calculated at the first order in ϕ ,

² A priori, the remapping function should depend not only on a convergence field but also on a rotation field, so that the deflection angle is not purely gradient but have a rotational contribution. However, Hirata & Seljak (2003b) have shown that rotation field effect would be negligible for the next generation of CMB experiments.

writes (Okamoto & Hu 2003):

$$\langle \tilde{T}(\mathbf{k}_1) \tilde{T}(\mathbf{k}_2) \rangle_{\text{CMB}} = (2\pi)^2 \delta(\mathbf{k}_1 + \mathbf{k}_2) \tilde{C}_{k_1}^{\text{TT}} + f_{\text{TT}}(\mathbf{k}_1, \mathbf{k}_2) \phi(\mathbf{L}) + O(\phi^2) \quad (4)$$

where $\mathbf{L} = \mathbf{k}_1 + \mathbf{k}_2$, and the CMB subscript denotes an ensemble average over different realisations of the CMB but a fixed integrated potential field. The weighting function f_{TT} depends on the primordial temperature APS, such as:

$$f_{\text{TT}}(\mathbf{k}_1, \mathbf{k}_2) = \mathbf{L} \cdot \mathbf{k}_1 C_{k_1}^{\text{TT}} + \mathbf{L} \cdot \mathbf{k}_2 C_{k_2}^{\text{TT}}. \quad (5)$$

Similarly, one can calculate the four-point correlation function of the CMB temperature field – such as in Kesden et al. (2003). One finds that the trispectrum of the lensed temperature field – or equivalently, the connected part of its four-point correlation function – is non-null even if the underlying (unlensed) temperature field is purely Gaussian.

For the sake of reconstructing the integrated gravitational potential field from a lensed CMB map, two methods exist in the literature. First, the quadratic estimator approach has been developed in Hu (2001b); Hu & Okamoto (2002); Okamoto & Hu (2003). Then a maximum-likelihood estimator method has been derived in Hirata & Seljak (2003a,b). The latter approach may increase the capabilities of the highest sensitivity highest resolution CMB projects in reconstructing the integrated potential while the former method is still very close to the optimality for current built experiment such as PLANCK. Thus we adopt the quadratic estimator throughout this work.

In the flat sky approximation, the estimated potential map takes the following form (Okamoto & Hu 2003):

$$\hat{\phi}_{\text{TT}}(\mathbf{L}) = \frac{A_{\text{TT}}(\mathbf{L})}{L^2} \int \frac{d^2 \mathbf{k}_1}{(2\pi)^2} \tilde{T}(\mathbf{k}_1) \tilde{T}(\mathbf{k}_2) F_{\text{TT}}(\mathbf{k}_1, \mathbf{k}_2), \quad (6)$$

where the Fourier modes $\tilde{T}(\mathbf{k})$ refer to the *observed* temperature modes, affected by both the CMB lensing and the instrumental noise of the CMB experiment concerned. More precisely, the temperature map is assumed to be contaminated by an additional white Gaussian noise and deconvolved from a beam function assumed to be Gaussian, so that its APS reads:

$$\langle \tilde{T}(\mathbf{k}_1) \tilde{T}(\mathbf{k}_2) \rangle = (2\pi)^2 \delta(\mathbf{k}_1 + \mathbf{k}_2) \left(\tilde{C}_{k_1}^{\text{TT}} + N_{k_1}^{\text{TT}} \right), \quad (7)$$

where $N_{k_1}^{\text{TT}}$ is the instrumental noise APS, modeled in this analysis as:

$$N_k^{\text{TT}} = \theta_{\text{fwhm}}^2 \sigma_{\text{T}}^2 \exp \left[k^2 \frac{\theta_{\text{fwhm}}^2}{8 \ln 2} \right], \quad (8)$$

where θ_{fwhm} is the full-width at half maximum (FWHM) of the beam function and σ_{T} , the root mean square of the noise per resolution elements.

Besides, the normalisation function is calculated so that $\hat{\phi}_{\text{TT}}(\mathbf{L})$ is an unbiased estimator of the integrated potential field:

$$A_{\text{TT}}(\mathbf{L}) = L^2 \left[\int \frac{d^2 \mathbf{k}_1}{(2\pi)^2} f_{\text{TT}}(\mathbf{k}_1, \mathbf{k}_2) F_{\text{TT}}(\mathbf{k}_1, \mathbf{k}_2) \right]^{-1}. \quad (9)$$

Then, the weighting function F_{TT} is adjusted to minimize the dominant contribution to the estimator variance, i. e. the unconnected part of the quantity $\langle \hat{\phi}_{\text{TT}}(\mathbf{L}) \hat{\phi}_{\text{TT}}(\mathbf{L}') \rangle - (2\pi)^2 \delta(\mathbf{L} + \mathbf{L}') C_L^{\phi\phi}$. Derived in Okamoto & Hu (2003), the calculation leads to:

$$F_{\text{TT}}(\mathbf{k}_1, \mathbf{k}_2) = \frac{f_{\text{TT}}(\mathbf{k}_1, \mathbf{k}_2)}{2 \tilde{C}_{k_1}^{\text{TT}} \tilde{C}_{k_2}^{\text{TT}}}, \quad (10)$$

where $\tilde{C}_k^{\text{TT}} \equiv \tilde{C}_k^{\text{TT}} + N_k^{\text{TT}}$ is the *observed* temperature power APS as defined in Eq. (7).

Finally, the covariance of the integrated potential field estimator provides us with a four-point estimator of the integrated potential APS. When expanding the lensed CMB temperature modes at second order in ϕ , the $\hat{\phi}_{\text{TT}}$ estimator covariance reads:

$$\langle \hat{\phi}_{\text{TT}}(\mathbf{L}) \hat{\phi}_{\text{TT}}(\mathbf{L}') \rangle = (2\pi)^2 \delta(\mathbf{L} + \mathbf{L}') C_{\text{TT,TT}}^{\phi\phi}(\mathbf{L}), \quad (11)$$

where the estimated potential APS, $C_{\text{TT,TT}}^{\phi\phi}(\mathbf{L})$, taking into account all sources of variances, both projected potential and CMB cosmic variance, instrumental noise and confusion noise from other potential Fourier modes, writes:

$$C_{\text{TT,TT}}^{\phi\phi}(\mathbf{L}) = C_L^{\phi\phi} + N_{(0)}^{\phi\phi}(\mathbf{L}) + N_{(1)}^{\phi\phi}(\mathbf{L}) + N_{(2)}^{\phi\phi}(\mathbf{L}). \quad (12)$$

Here, we have distinguished three different noise contributions to the integrated potential estimator variance. The dominant noise contribution, $N_{(0)}^{\phi\phi}(\mathbf{L}) = A_{\text{TT}}(\mathbf{L})$, depends only on the unlensed and the observed temperature APS. It represents the Gaussian contribution to the potential APS estimator, in a sense that it is the variance one would obtain by replacing the lensed temperature map in Eq. (6), by a map with the same APS but Gaussian statistics. In addition, the potential APS estimator suffers from sub-dominant non-Gaussian noise contributions. The first, quoted $N_{(1)}^{\phi\phi}(\mathbf{L})$ has been calculated by Kesden et al. (2003). The second non Gaussian noise term $N_{(2)}^{\phi\phi}(\mathbf{L})$ is quadratic in $C_L^{\phi\phi}$. First calculated in Hanson et al. (2009), this term is shown to contribute even more than the first-order one at low multipoles ($L \leq 200$).

These two non Gaussian noise terms arise from the trispectrum part (or so-called connected part) of the four-point lensed temperature correlator hidden in the integrated potential field estimator covariance. It can be interpreted as the confusion noise coming from other integrated potential modes. Since it depends on the integrated potential APS, which has to be estimated, an iterative estimation scheme would be required for taking it into account. However, our study based on simulated data allows us to calculate these terms from the fiducial potential APS and then subtract it from the estimator variance.

3. Effect of foreground removal: a Monte-Carlo analysis

Up to now, no analysis has been performed to assess the effect of a component separation process on the CMB lensing extraction. The question we propose to address here is whether the lensing signal is preserved in the CMB map output by the component separation process. In order to get a first insight, we use a Monte-Carlo approach within the flat sky approximation.

3.1. Idealized PLANCK sky model

We create a simulation pipeline to generate some idealized synthetic patches of the sky for the PLANCK experiment. Our sky model is a linear uncorrelated mixture of the lensed CMB temperature and astrophysical components, which includes the Sunyaev-Zel'dovich effect, the thermal emission of the interstellar dust and the unresolved infrared point sources emission. In modeling these three components, we ensure to catch the dominant foreground emission features at the PLANCK-HFI frequencies. Then we add the nominal effects of the PLANCK-HFI instrument, modeled as a purely Gaussian shaped beam and a spatially uniform white Gaussian noise. Each hypothesis we adopt

is a crude model of the astrophysical contaminant and systematic effects that pollute the PLANCK data, and is intended to be a *demonstration model* for a study devoted to the impact of the component separation algorithms on the CMB lensing retrieval.

We generate four sets of 300 PLANCK-HFI synthetic patches of the sky, with instrumental noise and, when needed, with foreground emissions:

- Set I contains lensed CMB temperature maps generated from an unique fixed projected potential realisation and with the instrumental effects (beam and white noise);
- Set I-fg is built from set I. In addition, a fixed realisation of dust and SZ is added to each set I map;
- Set II is a set of lensed CMB temperature maps generated from 300 random realisations of the lenses distribution plus the instrumental effects;
- Set II-fg is built from set II. Each map of set II is superimposed with randomly picked dust and SZ maps.

Note that the point sources emission will be included afterward in our simulation pipeline, through a direct estimation of the point sources residuals after component separation as described in Sect. 3.2. Sets I and I-fg will serve at studying the projected potential *field* reconstruction, whereas sets II and II-fg will be used in the projected potential *angular power spectrum* (APS) estimates analysis. Hereafter, our method and its assumed hypothesis are detailed.

3.1.1. Lensed CMB temperature map

Once we have assumed the Gaussianity of the integrated potential field, the lensed CMB temperature simulation principle is straightforward as a direct application of the remapping Eq. (1). We start from the APS of both the temperature and the projected potential field as well as the cross-APS reflecting the correlation between the CMB temperature and the gravitational potential fields due to the Integrated Sachs-Wolfe (ISW) effect. Then we generate two Gaussian fields directly in the Fourier space, so that

$$T(\mathbf{k}) = \sqrt{C_{|k|}^{\text{TT}}} G_{(0,1)}^{(1)}(\mathbf{k}) \quad (13)$$

$$\phi(\mathbf{k}) = \sqrt{\frac{(C_{|k|}^{\text{T}\phi})^2}{C_{|k|}^{\text{TT}}}} G_{(0,1)}^{(1)}(\mathbf{k}) + \sqrt{C_{|k|}^{\phi\phi} - \frac{(C_{|k|}^{\text{T}\phi})^2}{C_{|k|}^{\text{TT}}}} G_{(0,1)}^{(2)}(\mathbf{k}),$$

where $G_{(0,1)}^{(1)}(\mathbf{k})$ and $G_{(0,1)}^{(2)}(\mathbf{k})$ are two independent realisations of a Gaussian field of zero mean and unit variance. Because of the typical scales of the deflection field – deflection angles are of the order of 2 or 3 arcmin (depending on the fiducial cosmological model) but correlated over several degrees on the sky – the generated maps should be both high resolution and extended over not too small sky area. We choose to produce some 12.5×12.5 square degrees maps of 2.5 arcmin of resolution, as a good trade-off between the quality of the simulated maps and the time needed to the generation and the analysis of these maps.

From CMB temperature and projected potential in the Fourier space, we calculate both the temperature and the deflection angles in the real space. The last step consists in performing the remapping of the primordial temperature map according to the deflection angles. Here is the technical point. Starting from a regular sample of a field (the underlying unlensed map), we have to extract an irregular sample of the same field (the lensed map) – the new directions where to sample from are given by

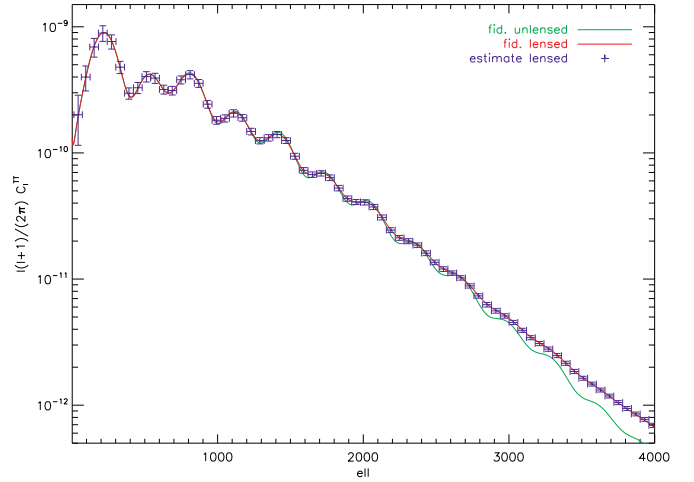


Fig. 1. CMB temperature APS. Red/black (respectively green/grey) line is the lensed (respectively unlensed) temperature APS calculated with the public Boltzmann code CAMB (Lewis et al. 2000; Challinor & Lewis 2005). The blue/black data-points are the mean of the binned power spectrum reconstructed on 500 simulated lensed temperature maps. The error-bars are given by the variance of the 500 APS estimates.

the previous one shifted by the deflection angles. Thus, this is a well-documented interpolation issue, the difficulty lying in the fact that the scale of the interpolation scheme is the same than the typical scale of the physical process under interest. We have to take particular care in the interpolation algorithm to avoid creating some spurious lensing signal or introducing additional non-Gaussianities. We find that a parametric cubic interpolation scheme (Park & Schowengerdt 1983) apply reasonably well. In addition, to avoid any loss of power due to the interpolation, we overpixelize twice the underlying unlensed temperature and deflection field. The first test we perform to control the quality of the simulation is to compare the Monte-Carlo estimate of the APS over 500 simulations of the lensed maps with the analytical calculation of the lensed APS provided by the CAMB³ Boltzmann code (Lewis et al. 2000; Challinor & Lewis 2005). As shown in Fig. 1, the APS of our simulated lensed maps is consistent with the theoretical one up to multipole 4000 – which is largely enough to study the CMB lensing with PLANCK.

3.1.2. Astrophysical components

In any CMB experiment the temperature signal is mixed with foreground contributions of astrophysical origin – among them we can separate the diffuse galactic emission (thermal and rotational dust, synchrotron, Bremsstrahlung (free-free) radiation) from the extragalactic components (point sources, thermal and kinetic Sunyaev-Zel’dovich effects). As discussed in the introduction, each of these components could potentially, if inefficiently removed, degrade our capability to reconstruct the CMB lensing. Here, to complete our demonstration sky model, we choose to simulate the dominant astrophysical foregrounds at the PLANCK-HFI frequencies, namely the thermal emission of the galactic dust, the thermal SZ effect and the unresolved infrared point sources. Thermal dust simulations are obtained from an interpolation of the $100\mu\text{m}$ IRAS data, in the sky region lo-

³ web site: <http://camb.info/>

cated around $\alpha = 204^\circ$ and $\delta = 11^\circ$, at the relevant CMB frequencies as described in Delabrouille et al. (2003). Note that several treatments have been applied on these maps – point sources removal, destripping, inpainting in the Fourier space with constraint realisations – which may induce an amount of additional non-Gaussianities. The SZ emission on the sky patches can be randomly selected in a set of 1500 realisations produced with a semi-analytical simulation tool provided in the literature (Delabrouille et al. 2002). Note that SZ emission is assumed here not to correlate with the CMB lensed signal. As for the estimates of the unresolved point sources residuals, we choose to take advantage of the refined full-sky simulations of the infrared point sources emission in each PLANCK-HFI frequencies, provided by the PLANCK *Component Separation Working Group* (WG2). In these simulations, the source counts are drawn from the IRAS catalog, and their spectral energy distributions are modeled following Serjeant & Harrison (2005). In addition, they involve several refinements, such as the filling of the IRAS mask by synthetic data, the additional simulation of fainter sources according to the Granato et al. (2004) model, and their clustering (see Leach et al. (2008)). Note that the radio-galaxies, another population of extragalactic sources, can be safely neglected here, as they lead to a sub-dominant emission compared to the infrared-galaxies one, at the PLANCK-HFI frequencies.

3.1.3. PLANCK-like noise

Finally, we simulate the effects of the PLANCK High Frequency Instrument (HFI) according to their nominal characteristics (The Planck Consortia 2005), which are summarized in Table 1. At each frequency channel, the component mixture is convoluted by a Gaussian beam with the corresponding FWHM size. Then a spatially uniform white noise following a Gaussian statistic is added. Finally, the resulting maps can be deconvolved from the beam transfer function, resulting in an exponential increase of the noise at the scales corresponding to the beam size. Because smaller angular scale carry the larger amount of lensing information, the higher the angular resolution is, the better the lensing reconstruction can be. Our tests show that in the ideal case, the lensing reconstruction on PLANCK-HFI synthetic maps is insensitive to the addition or the removal of the 100 GHz frequency channel information, whose beam function is roughly twice larger than the beam in the higher frequency channels. Worst, when running the full Monte-Carlo chain, turning on the foreground emissions and the component separation process, adding the lower frequency channel results in increasing the confusion noise of the lensing reconstruction. That’s why, we exclude the 100 GHz frequency channel of our analysis. To summarize, our PLANCK sky model reads:

$$\mathbf{T}^{\text{obs}} = \mathcal{A} \mathbf{s} + \mathbf{B}^{-1} \otimes \mathbf{n}, \quad (14)$$

where \mathbf{T}^{obs} is the set of five individual frequency channel maps, \mathcal{A} is the mixing matrix calculated from the frequency dependence of the three signal contributions, \mathbf{s} is the set of CMB, dust and SZ maps at a pivot frequency, \mathbf{B}^{-1} is the set of Gaussian beam inverse transfer functions and \mathbf{n} , the set of white noise maps in the five frequency channels we have selected. Note that we assume a perfect beam deconvolution process.

3.2. Component separation using GMCA

For most of the cosmological analysis of the CMB data – and for the CMB lensing extraction in particular – the cosmological

Table 1. Instrumental characteristics of PLANCK-HFI^a

channel (GHz)	θ_{fwhm} (arcmin)	σ_{T} ($\mu\text{K}^2 \cdot \text{sr}^{-1}$)
100	9.5	6.8
143	7.1	6.0
217	5.	13.1
353	5.	40.1
545	5.	401
857	5.	18 300.

^a (see The Planck Consortia 2005)

signal has to be carefully disentangled from the other sources of emission that contribute to the observed temperature map. The component separation is a part of the signal processing dedicated to discriminate between the different contributions of the final maps. Briefly, the gist of any component separation technique consists in taking profit of the difference in the frequency behavior and the spatial structures (i.e. morphology) that distinguish these different *components*. From a set of frequency channel maps, a typical component separation algorithm provides a unique map of the CMB temperature with the instrumental noise and a foreground emission residual. In general, the lower the foreground residual rms level the better the separation algorithm. However, this simple rule is not necessarily true for CMB lensing reconstruction. In this case, preserving the statistical properties of the underlying CMB temperature map is critical.

In the PLANCK consortium, the component separation is a critical issue, involving a whole Working Group (WG2) devoted to provide several algorithms for separating CMB from foregrounds and to compare their merits (see Leach et al. (2008) for a recent comparison of the current proposed methods). Eight teams have provided a complete component separation pipeline capable to treat a realistic set of PLANCK temperature and polarization maps. Each methods differ in the external constraints they use, the physical modeling they assume and the algorithm they are based on.

Among the available techniques, we choose to use the Generalized Morphological Component Analysis (hereafter GMCA) which is a blind method component separation method. In GMCA, each observation $\mathbf{T}_v^{\text{obs}}(\hat{\mathbf{n}})$ is assumed to be the linear combination of n_c *components* $\{s^i(\hat{\mathbf{n}})\}_{i=1, \dots, n_c}$ such that:

$$\mathbf{T}_v^{\text{obs}}(\hat{\mathbf{n}}) = \mathcal{A}_{vi} s^i(\hat{\mathbf{n}}) + \mathbf{n}_v(\hat{\mathbf{n}}), \quad (15)$$

where $\mathbf{n}_v(\hat{\mathbf{n}})$ models instrumental noise. The general idea subtending this algorithm is the fact that the components, which result from completely different physical processes, have different spatial morphologies or structures. These morphological differences translate into a difference in their representation into a fixed waveform dictionary \mathcal{D} . If only a few coefficients of a fixed dictionary are enough to completely represent a given component, this component is said to be sparse in that dictionary \mathcal{D} . The dictionary succeeds in catching the general features that characterize the component morphology. That’s why, separating the observed map into components that maximize their sparsity in a given dictionary is an efficient strategy to distinguish between physically different emission sources. In practice, a wavelet basis is a good choice for astrophysical components that overwhelmingly contain smooth spatial features. GMCA is a sparsity-maximization algorithm, a notion that we briefly introduce hereafter. Let $\{d^j(\hat{\mathbf{n}})\}$ be the set of vector that forms the dictionary \mathcal{D} . Let $\alpha_{ij} = \langle s^i(\hat{\mathbf{n}}), d^j(\hat{\mathbf{n}}) \rangle$ denote the scalar product

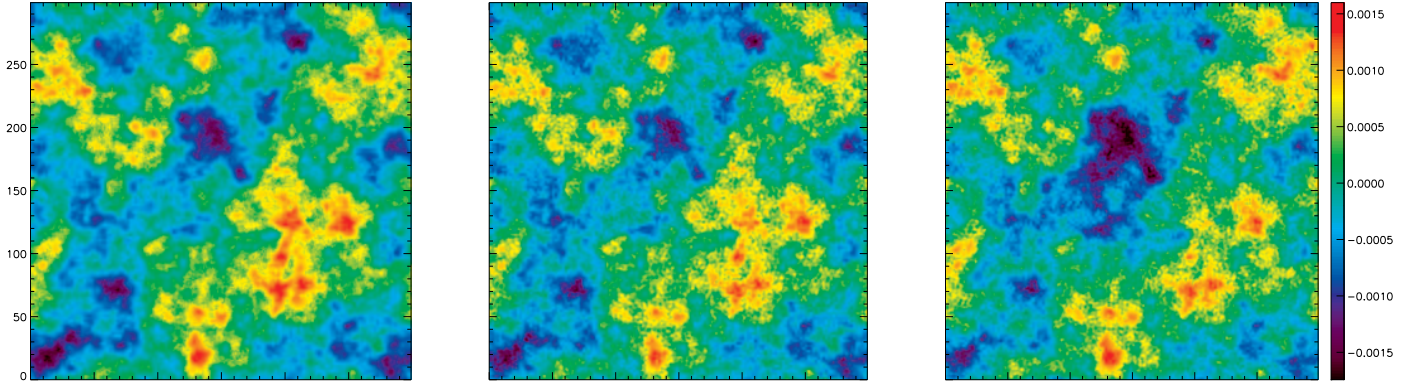


Fig. 2. Impact of the foregrounds residuals on the deflection field reconstruction on $12.5^\circ \times 12.5^\circ$ square patches. Left: the input realisation of the deflection amplitude; Middle: the stack of 300 deflection estimates from the set I maps (synthetic PLANCK temperature maps – without any foregrounds residuals); Right: the stack of 300 deflection estimates from the set I-GMCA maps (PLANCK temperature maps output of the GMCA component separation process). All maps have the same color table shown in the right-most part of the figure.

coefficients between $s^i(\hat{\mathbf{n}})$ and $d^j(\hat{\mathbf{n}})$. When \mathcal{D} is an orthogonal wavelet basis, the following properties hold :

$$\begin{aligned} \langle d^i(\hat{\mathbf{n}}), d^j(\hat{\mathbf{n}}) \rangle &= 0 \text{ if } i \neq j \\ \langle d^i(\hat{\mathbf{n}}), d^i(\hat{\mathbf{n}}) \rangle &= 1 \\ s^i(\hat{\mathbf{n}}) &= \sum_j \langle s^i(\hat{\mathbf{n}}), d^j(\hat{\mathbf{n}}) \rangle d^j(\hat{\mathbf{n}}) \end{aligned}$$

Then GMCA estimates the components $\{s^i(\hat{\mathbf{n}})\}$ and the mixtures weights $\{\mathcal{A}_{vi}\}$ by maximizing the sparsity of each component in \mathcal{D} . As advocated in Bobin et al. (2008), a good sparsity estimate is the sum of the absolute values of $\{\alpha_{ij}\}_{i,j}$. Maximizing the sparsity of the components is then equivalent to minimizing this sparsity measure. The model parameters are estimated by GMCA as follows:

$$\min_{\{s^i(\hat{\mathbf{n}})\}, \{\mathcal{A}_{vi}\}} \sum_{ij} |\alpha_{ij}| \text{ s.t. } \|\mathbf{T}_v^{\text{obs}}(\hat{\mathbf{n}}) - \mathcal{A}_{vi} s^i(\hat{\mathbf{n}})\| < \epsilon \quad (16)$$

where ϵ stands for the reconstruction error. The norm $\|\cdot\|$ stands for the usual ℓ_2 norm:

$$\|\mathbf{T}_v^{\text{obs}}(\hat{\mathbf{n}}) - \mathcal{A}_{vi} s^i(\hat{\mathbf{n}})\| = \sqrt{\sum_{v,i,\hat{\mathbf{n}}} (\mathbf{T}_v^{\text{obs}}(\hat{\mathbf{n}}) - \mathcal{A}_{vi} s^i(\hat{\mathbf{n}}))^2} \quad (17)$$

GMCA estimates the components $\{s^i(\hat{\mathbf{n}})\}$ which have only a few significant coefficients $\{\alpha_{ij}\}$ in the dictionary; i.e. the components which are sparse in \mathcal{D} . Further technical details are given in Bobin et al. (2008).

For PLANCK, the parameter ϵ is chosen to be very small. In that case, the components $\{s^i(\hat{\mathbf{n}})\}$ are estimated by applying the pseudo-inverse of the mixing matrix \mathcal{A} to the observation channels $\{\mathbf{T}_v^{\text{obs}}(\hat{\mathbf{n}})\}$:

$$s^i(\hat{\mathbf{n}}) = \sum_v \mathcal{A}_{vi}^+ \mathbf{T}_v^{\text{obs}}(\hat{\mathbf{n}}) \quad (18)$$

where \mathcal{A}_{vi}^+ is the element at position $\{i, v\}$ of the pseudo-inverse matrix of \mathcal{A} defined as: $\mathcal{A}^+ = (\mathcal{A}^T \mathcal{A})^{-1} \mathcal{A}^T$. Interestingly, the contribution of the component separation is then linear. As a consequence, the noise perturbing each component can be accurately known. Furthermore, the linearity of the separation guarantees that the separation technique itself does not generate non-Gaussianity in estimated CMB map. Only the residual terms

coming from the other components can create non-Gaussian features in the CMB.

Another important consequence is that these properties give us a conservative method to estimate the point sources residuals remaining within the CMB maps after foreground cleaning, as describe hereafter. Because each source has its own spectral property, component separation techniques fail at disentangling the point sources emission from the observed maps. As a result, point sources remain mixed with the other components and the precise amount of the point sources emission by observation channels which has leaked in each component, is determined by the coefficients of the mixing matrix. More formally, in order to estimate the point sources residuals embedded in the foreground-cleaned CMB maps, quoted $s^{\text{ps}}(\hat{\mathbf{n}})$, one can apply Eq. 18 to the simulated point sources in the observation channels $\{\mathbf{T}_v^{\text{ps}}(\hat{\mathbf{n}})\}$:

$$s^{\text{ps}}(\hat{\mathbf{n}}) = \sum_v \mathcal{A}_{v0}^+ \mathbf{T}_v^{\text{ps}}(\hat{\mathbf{n}}) \quad (19)$$

where the elements $\{\mathcal{A}_{v0}^+\}$ form the column of the pseudo-inverse matrix which corresponds to the CMB component. Then the brighter point sources, which have been previously detected in the PLANCK-HFI channels, are masked out and the corresponding gaps are restored using an *inpainting* method. A detailed description of the mask and the restoration technique will be given hereafter in the Sect. 4. The final full-sky map we obtain is an estimate of the unresolved infrared point sources residuals, which contaminate the CMB temperature map after component separation with GMCA. This sky map is divided into patches of 12.5×12.5 square degrees with 50% overlapping. We form a set of 300 point sources residuals square maps by selecting the patches with a maximal 30% masked area.

We perform the component separation using GMCA on sets I-fg and II-fg, each of 300 simulated patches generated following our idealized PLANCK sky model and described in the previous section (3.1). As an output of this process, we obtain two sets of 300 foreground-cleaned CMB temperature maps. Note that GMCA achieves the extraction of the foreground components as well. Unresolved point sources residuals are added to each map of these two sets. In the following, we will refer to the sets of lensed CMB maps with galactic dust, SZ effect and point sources residuals after the GMCA component separation, as sets I-GMCA and II-GMCA respectively.

3.3. CMB lensing reconstruction

Here, we apply a discrete version of the quadratic estimator written by Okamoto & Hu (Eq. 6) on the different sets of simulated maps previously described, namely sets I, I-GMCA, II and II-GMCA. We seek to assess the foreground residuals impact on our capability to reconstruct CMB lensing with PLANCK.

3.3.1. Testing the estimator performances

First, we give explicitly the expression of the discrete quadratic estimator that we derive from Eq. (6):

$$\hat{\phi}_{\text{TT}}(\mathbf{U}) = \frac{A_{\text{TT}}(L)}{L^2 A} \sum_{\mathcal{D}_1 \cap \mathcal{D}_2} \bar{T}(\mathbf{u}_1) \bar{T}(\mathbf{u}_2) F_{\text{TT}}(\mathbf{u}_1, \mathbf{u}_2), \quad (20)$$

where \mathbf{U} , \mathbf{u}_1 and \mathbf{u}_2 are wave-vectors related by $\mathbf{u}_1 + \mathbf{u}_2 = \mathbf{U}$ and A is the area of the sky patch considered. The sum is performed on the intersection of two disks \mathcal{D}_1 and \mathcal{D}_2 . The former is the zero-frequency centered disk defined by $\Delta_1 |\mathbf{u}_1| \leq L_{\text{max}}$, where Δ_1 denotes the frequency interval in the Fourier space (i.e. the smallest nonzero positive frequency), which equals $2\pi/\sqrt{A}$. The latter, namely \mathcal{D}_2 , is also a disk of radius L_{max} but centered around \mathbf{U} . It is therefore defined by $\Delta_1 |(\mathbf{u}_2 - \mathbf{U})| \leq L_{\text{max}}$. The wave-vectors \mathbf{u}_1 , \mathbf{u}_2 and \mathbf{U} correspond to \mathbf{k}_1/Δ_1 , \mathbf{k}_2/Δ_1 and \mathbf{L}/Δ_1 respectively. The normalisation $A_{\text{TT}}(L)$ and the weighting function $F_{\text{TT}}(\mathbf{u}_1, \mathbf{u}_2)$ are respectively the discrete version of Eq. (9) and Eq. (10). For the PLANCK-HFI experiment, we verify that the reconstructed potential field does not vary either we cut the sum in Eq. (20) at $L_{\text{max}} = 2600$ or we push it further.

We study our capability to reconstruct a map of the integrated potential field with PLANCK-HFI idealized simulation, assuming a perfect component separation without any foreground residuals. We apply the discrete quadratic estimator on set I maps (see Sect. 3.1) to obtain 300 estimates of the same realisation of the projected potential field ϕ . Once stacking these estimates, the final ϕ map is an estimate of the input ϕ realisation. Following Hu (2001b), we prefer to present our results in terms of the deflection field amplitude rather than the very smooth gravitational potential field, in order to highlight the intermediate angular scales features. Fig. 2 shows the input deflection field realisation, which has been used to simulate the lensing effect in the set I maps (on the first panel), as well as its reconstruction with the quadratic estimator applied on the set I maps (second panel). Even if the reconstruction noise is visible at smaller angular scales, the features of the deflection map are well recovered.

Characterizing PLANCK sensitivity to the projected potential APS requires to account for both the CMB and the projected potential field cosmic variances. Thus, we move on to set II. As previously, we apply the quadratic estimator (Eq. 20) on the lensed CMB maps to reconstruct projected potential fields. Averaging over the APS of these individual ϕ field estimates gives an evaluation of the quadratic estimator variance (as defined in Eq. 11). The final reconstructed projected potential APS is obtained in subtracting the noise contributions, described in Sect. 2, from the variance. The former is related by Eq. (3) to the deflection APS shown in the Fig. 3. The error bars are estimated as the dispersion between each individual deflection APS reconstruction. Thus, set II maps, which are idealized versions of the PLANCK-HFI sky assuming a perfect component separation, lead to a good reconstruction of the deflection APS up to $L_{\text{max}} = 2600$. The error-bars evaluated here give an upper limit of the PLANCK-HFI sensitivity to the deflection APS. As one can see on Fig. 4,

they are compatible with the theoretical 1σ error-bars one can calculate from the Fisher formalism:

$$\Delta C_L^{\text{dd}} = \sqrt{\frac{1}{N_{\text{eff}}}} (C_L^{\text{dd}} + N_L^{\text{dd}}), \quad (21)$$

where $N_{\text{eff}} = 4\pi/L\Delta LA$ is a naive estimate of the independent available Fourier modes. The error bars estimated here will provide us with a comparison level to quantify the impact of the foreground residuals.

3.3.2. Impact of the foreground residuals

Here we essentially redo the same analysis but using the full-simulation pipeline of our PLANCK-HFI demonstration model. The integrated potential field is extracted from the sets I-GMCA and II-GMCA described in Sect. 3.2.

First, we aim at developing an intuition on the impact of foreground residuals on the deflection map reconstruction. We use the set I-GMCA, in which both deflection field and foregrounds realisations are fixed. As previously, the 300 deflection field estimates reconstructed with the quadratic estimator are stacked to produce a unique reconstructed deflection field shown in Fig. 2. We can see that the recovery of the underlying deflection field is still achieved even in presence of foreground emission and after the GMCA analysis. The impact of the foreground residuals is nevertheless visible, mostly at angular scales larger than 2 degrees whereas the intermediate angular scale features seem more preserved.

For a more quantitative analysis, we move on to the impact of the foreground residuals on the deflection APS reconstruction. We use the set II-GMCA (see Sects. 3.1 and 3.2) to ensure that the variances of the CMB, the deflection field and the foregrounds are accounted for. We reconstruct a deflection field estimate from each of the set II-GMCA maps using the quadratic estimator given in Eq. (20). Finally, we obtain the reconstructed deflection APS from the average variance over these 300 deflection APS estimates as described in Sect. 3.3.1.

The reconstructed binned deflection APS with the evaluated 1σ errors is represented in the Fig. 3. Fig. 4 shows the difference between the reconstructed and the input deflection APS. First we report that the foreground residuals does not compromise the PLANCK-HFI capability to reconstruct the deflection APS – or equivalently the integrated potential APS. Fig. 3 shows that the APS reconstruction is preserved at the angular scales from $L = 60$ up to $L = 2600$. In this multipole range, the GMCA algorithm succeeds in letting unchanged the statistical properties of the lensed CMB temperature anisotropies, which suggests that this is a well-appropriated component separation tool for CMB lensing reconstruction. As for the first multipole bin, we report a 4σ excess of the deflection signal in the $L = 2$ to $L = 60$ multipole range. We have checked that this bias is linked to the introduction of the unresolved point sources residuals in our simulation pipeline. Interestingly, we find that this excess originates not from the level of residuals themselves, but mostly from the cutting procedure⁴ we use to extract the set of 300 square maps from our full-sky point sources residuals. We postpone a closer inspection of the low multipole lensing reconstruction behavior

⁴ The cutting procedure involves a sphere-to-plan projection, an apodisation and a fit of the Fourier coefficients of the square map. From the tests we run (not presented here), the apodisation appears to have the most harmful impact on the high angular scale deflection reconstruction. A complete study of the impact of the sphere to patches transition will be the subject of a companion paper.

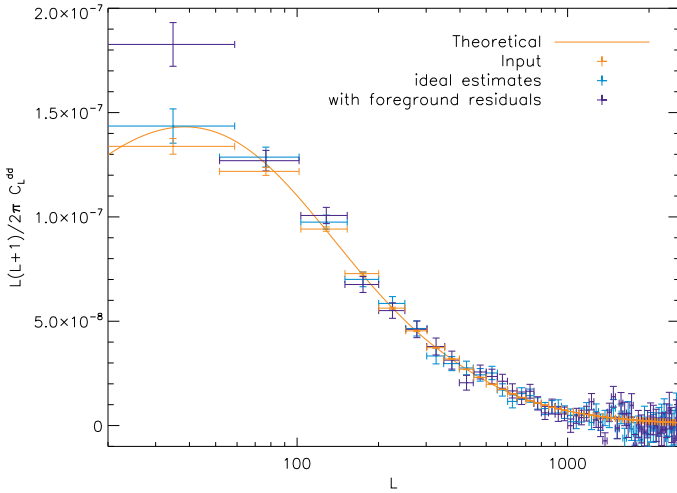


Fig. 3. The deflection APS. Data-points are the binned APS reconstructed from PLANCK synthetic lensed CMB maps in two cases: (light blue/grey) the *ideal* case without any foregrounds and (dark blue/black) the case with foreground residuals from the GMCA output CMB maps. The fiducial deflection APS calculated with CAMB is figured by the (orange/solid) line; Orange/grey data points are the binned deflection APS estimates on the 300 input deflection field realisations. The horizontal and vertical intervals associated with the data points represent the averaging multipole bands and the 1σ errors respectively.

to the complete full-sky study (hereafter in Sect. 4). Apart from the excess signal in the first bin, the impact of the foreground residuals on the deflection reconstruction is also slightly visible at all angular scales, as seen in the Fig. 4. If the difference between reconstructed and input APS is still compatible with zero within the theoretical 1σ errors in the 60 to 2600 multipole range, this residual bias appears more featured, more oscillating than in the previous no foreground case. To quantify this degradation in the deflection APS reconstruction, we calculate the total error in unit of σ , defined as:

$$\Delta = \sum_b \left| \frac{\hat{C}_b^{dd} - C_b^{dd}}{\sigma_b} \right|, \quad (22)$$

where \hat{C}_b^{dd} and C_b^{dd} are respectively the reconstructed and input deflection APS in the b frequency band, and σ_b the 1σ error on \hat{C}_b^{dd} . Note that when evaluating the total error, we exclude the first bin bias, which has been discussed previously. With this definition, we find a total error, $\Delta_{\text{ideal}} = 33$, in the no foregrounds case whereas $\Delta_{\text{gmca}} = 41$, in presence of GMCA foreground residuals. If the total error serves as quantifying the increase of the *bias* of the deflection APS reconstruction, one can also evaluate the increase of the *errorbars*. We find that the presence of foreground residuals results in a 10% increase of the errorbars on average. It suggests that at least an amount of the non-Gaussian foreground residuals is mixed up with the lensing signal in the reconstruction process. Foregrounds showing some small angular scale (around 15 to 5 arcmin) features – such as concentrated dust emission or brightest SZ clusters and point sources smeared by the instrument beam function – are potentially the more challenging for the CMB lensing reconstruction. In addition, we remind that our sky model is intended to catch the dominant foreground features at the PLANCK-HFI frequencies. The sub-dominant existing emissions, as free-free or

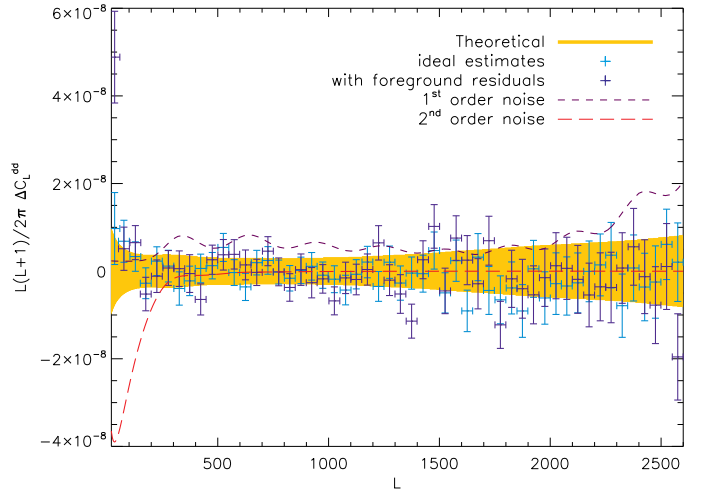


Fig. 4. Residual bias of the deflection APS reconstruction. Data-points figure the difference between the reconstructed and the input deflection APS averaging over 300 estimates: in the *ideal* case in light blue/grey and in the case with foreground residuals in dark blue/black (consistently with the Fig. 3 caption). The lines show the non-Gaussian noise terms of the quadratic estimator, at the first-order (violet/dashed) and at the second-order (red/long dashed) in C_L^{dd} . Orange/grey colored band is the analytical 1σ error band derived from the Fisher formalism.

synchrotron emissions, may marginally degrade our results as they are expected to slightly increase the foregrounds residuals within the CMB map.

As a final remark, we note that, because of the first bin excess signal problem, linked to the sphere to patches transition, one might privilege a full-sky approach when seeking at a precise lensing reconstruction at the higher ($L < 60$) angular scales.

4. Impact of masks on the full-sky lensing reconstruction

4.1. Introduction

From now, we move to a full-sky analysis of the CMB lensing effect. Some large area of the map, where the CMB signal is highly dominated by the foreground emission (e. g. the galactic plane, the point sources directions), have to be masked out. Cutting to zero introduces some mode-coupling within the CMB observables. As the lensing reconstruction methods rely on the off-diagonal terms of the CMB data covariance matrix, the map-masking yields some artifacts in the projected potential estimate if not accounted for. Several methods have been proposed to treat the masking effect for extracting the lensing potential field from the WMAP data. In Smith et al. (2007), the reconstruction is performed on the least-square estimate of the signal given the all-channels WMAP temperature data, requiring the inversion of the total data covariance matrix ($S + N$). However, as relying at least on the inversion of the noise covariance matrix, such an optimal data filtering approach is very CPU-consuming when applied to the WMAP maps. The PLANCK-HFI resolution enables to provide 50 Mega pixels maps. Thus, the previous method to account for the masking will be difficult to extend to PLANCK. In Hirata et al. (2008), the need for dealing with the noise covariance matrix is avoided by cross-correlating different frequency band maps. However, this method implies that no component

separation has been performed on the CMB maps before the lensing extraction. As a result, a lot of non-Gaussianities of foreground emission origin yields some artifact in the projected potential estimate, requiring a challenging post-processing to be corrected out. As previously mentioned, the PLANCK collaboration devotes strong efforts in the component separation activities and the current developed methods have already proved their efficiency (Leach et al. 2008). Moreover, the results we obtained with the *demonstration analysis* (see Sect. 3) tend to indicate that the lensing reconstruction is still doable after a component separation. Hence we plan to exploit the PLANCK frequency band maps to clean out the foreground emission before reconstructing the lensing potential rather than using the cross-correlation based lensing estimator. As a consequence, we need an alternative method to solve the masking issue in maps at the PLANCK resolution. Here, we propose to use an *inpainting* method, assess its impact on the CMB lensing retrieval and check its robustness to the presence of foregrounds residuals within the CMB map.

First, we describe the hypothesis assumed and the tools we use to generate synthetic all-sky lensed temperature maps for PLANCK. Then we describe our full-sky lensing estimator and test its performances on some PLANCK-like temperature maps. Finally, we review the *inpainting* method and conclude in studying the effect of the *inpainting* on the projected potential APS reconstruction in two cases, first assuming a perfect component separation then in presence of point sources residuals.

4.2. Full-sky simulation

The formalism reviewed in Sect. 2 is almost fully applicable to the spherical case. In particular, the remapping equation (Eq. 1) still holds, so that a lensed CMB sphere is given by:

$$\widehat{T}(\hat{n}) = T(\hat{n} + \nabla\phi(\hat{n})), \quad (23)$$

where the ∇ operator is to be understood as the covariant derivative on the sphere (Lewis & Challinor 2006). $\nabla\phi$ is identified to be the deflection field \mathbf{d} . Its zenithal and azimuthal coordinates can be calculated as the real and imaginary parts of a complex spin one field, using spin-weighted spherical harmonics transform – the detailed calculation can be found in Hu (2000) and Lewis (2005).

The LENSPIX⁵ package described in Lewis (2005) aims at generating a set of lensed CMB temperature and polarisation maps from the analytical auto- and cross-APS of $\{T, E, B, \phi\}$, the temperature, the E and B polarisation modes and the line-of-sight projected potential respectively. The maps are provided in the HEALPIX⁶ pixelisation scheme (Górski et al. 2005). The CMB lensing simulation is achieved in remapping the anisotropy fields according to Eq. (23) of a higher resolution map using a bicubic interpolation scheme in equi-cylindrical pixels. A lensed temperature map at the PLANCK resolution ($n_{\text{side}} = 2048$), can be computed in about 5 minutes on a 4-processors machine. The relative difference between the lensed temperature APS reconstructed on such a map and the analytical lensed APS obtained with CAMB⁷ (Lewis et al. 2000) is below 1% up to $l = 2750$. Here, to conservatively ensure a relative error below 1%, we choose a multipole cut at $L_{\text{max}} = 2600$. By its speed and pre-

cision quality, LENSPIX is a well adapted tool for a CMB lensing analysis with PLANCK data alone.

We obtained some PLANCK-HFI synthetic maps as the flat-sky case (see Sect. 3). White Gaussian noise realisations and Gaussian beam effect are added to the lensed temperature maps provided by the LENSPIX code. This Gaussian noise contribution is fully defined by the all-channels beam-deconvolved APS given by:

$$N_l^{\text{TT}} = \left(\sum_v \frac{1}{N_l^{\text{TT},v}} \right)^{-1}, \quad (24)$$

where $N_l^{\text{TT},v} = (\theta_{\text{fwhm}} \sigma_T)^2 \exp[l(l+1)\theta_{\text{fwhm}}^2/8 \ln 2]$, θ_{fwhm} and σ_T are the full width at half maximum of the beam and the level of white noise per resolution element respectively, as given in Table 1. The noise map is generated using the map creation tool of the HEALPIX package.

For the lensing reconstruction analysis, we prepare two sets of 50 all-sky maps with 1.7 arcmin of angular resolution (the HEALPIX resolution parameter $n_{\text{side}} = 2048$). In each set, maps are the *lensed* CMB temperature plus the PLANCK-HFI nominal Gaussian noise.

4.3. Full sky lensing reconstruction

We carry out an integrated potential estimation tool based on the full-sky version of the quadratic estimator derived in Hu (2001a). We closely follow the prescription given in Okamoto & Hu (2003) to build an efficient estimator, so that:

$$\widehat{\phi}_{LM} = \frac{N_L^{(0)}}{L(L+1)} \int d\hat{n} \left(T^{(\text{hp})}(\hat{n}) \nabla T^{(\text{w})}(\hat{n}) \cdot \nabla Y_{LM}^*(\hat{n}) \right), \quad (25)$$

where $T^{(\text{hp})}$ and $T^{(\text{w})}$ are respectively high-pass filtered and weighted lensed CMB temperature field, given by:

$$T^{(\text{hp})}(\hat{n}) = \sum_{lm} \frac{1}{\bar{C}_l^{\text{TT}}} \bar{T}_{lm} Y_{lm}(\hat{n}) \quad (26)$$

$$T^{(\text{w})}(\hat{n}) = \sum_{lm} \frac{C_l^{\text{TT}}}{\bar{C}_l^{\text{TT}}} \bar{T}_{lm} Y_{lm}(\hat{n}).$$

The covariant derivative operator ∇ applied on the spherical harmonics can be expressed in term of the spin ± 1 projectors $e_{\pm} = e_{\theta} \pm ie_{\phi}$ and the spin weighted spherical harmonics, as explained in Okamoto & Hu (2003). The quantities appearing in Eq. (25) can thus be calculated by direct and inverse (spin zero) spherical harmonics and spin-weighted (spin ± 1) spherical harmonics transforms. As for the estimator normalisation, quoted $N_L^{(0)}$, it identifies with the Gaussian contribution to the estimator variance; For its expression, we refer to Eq. (34) in Okamoto & Hu (2003). Then, extending to the spherical case the calculations reviewed in Sect. 2, the covariance of the integrated potential field estimator $\widehat{\phi}_{LM}$, averaged over an ensemble of CMB and gravitational potential fields realisations, depends on the potential APS, so that:

$$\langle \widehat{\phi}_{LM} \widehat{\phi}_{L'M'} \rangle = \delta_{LL'} \delta_{MM'} \left(C_L^{\phi\phi} + N_L^{(0)} + N_L^{(1)} + N_L^{(2)} \right), \quad (27)$$

where $N_L^{(0)}$, $N_L^{(1)}$ and $N_L^{(2)}$ are zeroth, first and second order in $C_L^{\phi\phi}$ noise terms respectively. To calculate the first sub-dominant noise term, one can use the expression derived in the flat-sky approximation by Kesden et al. (2003). Likewise, the second order term is given in Hanson et al. (2009). As these terms are an

⁵ <http://cosmologist.info/lenspix/>

⁶ The acronym for 'Hierarchical Equal Area isoLatitude Pixelization' of a sphere (see <http://healpix.jpl.nasa.gov/index.shtml>).

⁷ The 'Code for Anisotropies in the Microwave Background' is a so-called Boltzmann's code described at <http://camb.info/>

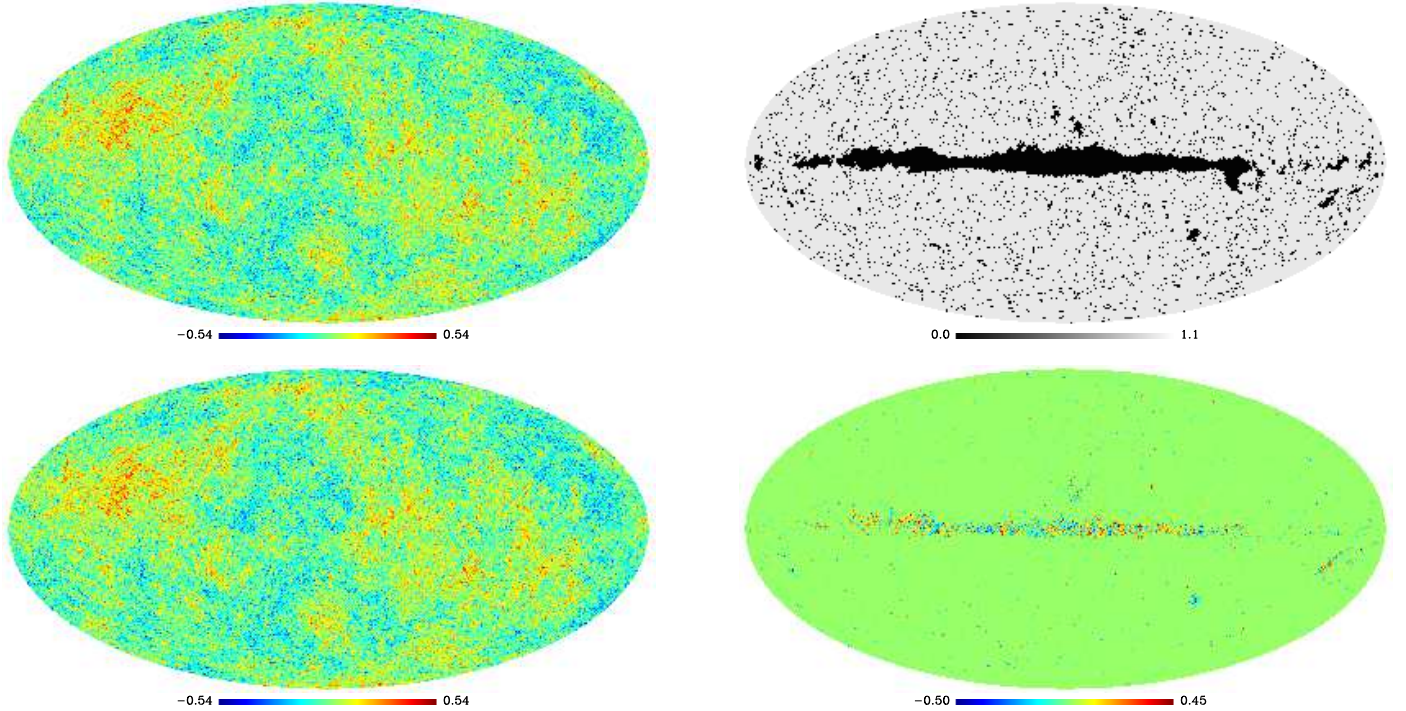


Fig. 5. All-sky maps in Galactic Mollweide projection. Upper panels: (left) a PLANCK-HFI synthetic CMB temperature map in milliKelvin, (right) the union mask defined in Sect. 4.5. The grey region shows the observed pixels whereas in black are the rejected ones. Lower panels: left panel shows the restored CMB map obtained by applying the *inpainting* process (described in Sect. 4.4) on the previous upper-left CMB map masked according to the union mask and the right panel shows the difference between the input (upper-left) CMB map and the restored (lower-left) one.

order of magnitude smaller than the dominant $N_L^{(0)}$ term and because the flat-sky approximation is known to be robust for the potential estimator noise calculation (Okamoto & Hu 2003), we assume and will verify that the deviation due to the flat-sky approximation is negligible.

Within the framework of Monte-Carlo analysis, we build a projected potential APS estimator so that:

$$\widehat{C}_L^{\phi\phi} = \frac{1}{N} \sum_{i=1}^N \left[\frac{1}{2L+1} \sum_M |\widehat{\phi}_{LM}^i|^2 \right] - (N_L^{(0)} + N_L^{(1)} + N_L^{(2)}), \quad (28)$$

where $\widehat{\phi}_{LM}^i$ is the integrated potential field estimate on the i^{th} CMB temperature realisation, $i \in \{1, \dots, N\}$. Note that since $N_L^{(1)}$ and $N_L^{(2)}$ depend on the potential APS itself, it should be evaluated and subtracted iteratively. Here we calculate it once from the theoretical integrated potential APS.

Finally, we test our APS estimator on a set of 10 lensed CMB temperature maps of 50 millions of pixels, including the nominal PLANCK noise, generated as described in Sect. 4.2. As in the flat-sky case, sums in the spherical harmonic space are cut at $L_{\text{max}}=2600$. The results, compiled in the form of an integrated potential APS estimate averaged over the 10 trials (see Eq. (28)), are shown in the left panels of Fig. 6.

4.4. Inpainting the mask

We choose to take into account the cutting effect of the temperature map before any lensing reconstruction rather than making any changes in the quadratic estimator (given in Eq. 25) to account for the mask. This approach is motivated by the fact that the high quality and the large frequency coverage of the PLANCK

data allow to reconstruct the CMB temperature map on roughly 90% of the sky. It therefore suggests that a method intended to fill the gap in the map can be applicable.

Several of such methods, referred to as *inpainting*, have been recently developed since the pioneering work of Masnou & Morel (1998). The general purpose of these methods is to restore missing or damaged regions of an image to retrieve as far as possible the original image. For the CMB lensing reconstruction, the ideal *inpainting* method would lead a restored map having the same statistical properties than the underlying unmasked map. To use a notion briefly mentioned in the section 3.2, the masking effect can be thought of as a loss of *sparsity* in the map representation: the information required to define the map has been spread across the spherical harmonics basis. That's why, the *inpainting* process can also be thought of as a restoration of the CMB temperature field *sparsity* in a conveniently chosen waveform dictionary. Elad et al. (2005) introduced a sparsity-based technique to fill in the missing pixels. This method has been extended to the sphere in Abrial et al. (2008, 2007). In a nutshell, the masked CMB map is modeled as follows :

$$\mathcal{T}(\hat{n}) = \mathcal{M}(\hat{n})T(\hat{n}) \quad (29)$$

where $\mathcal{M}(\hat{n})$ stands for a binary mask the entries of which are one when the pixel is observed and zero when it is missing. As emphasized in Elad et al. (2005); Abrial et al. (2008), if $T(\hat{n})$ has a sparse representation in a given waveform dictionary \mathcal{D} (see 3.2), masking is likely to degrade the sparsity the CMB map in \mathcal{D} . Let $\{d^j(\hat{n})\}$ be the set of vector that forms the dictionary \mathcal{D} . Let α_j denote the scalar product (so-called coefficients) between $T(\hat{n})$ and $d^j(\hat{n})$: $\alpha_j = \langle T(\hat{n}), d^j(\hat{n}) \rangle$. For the sake of simplicity,

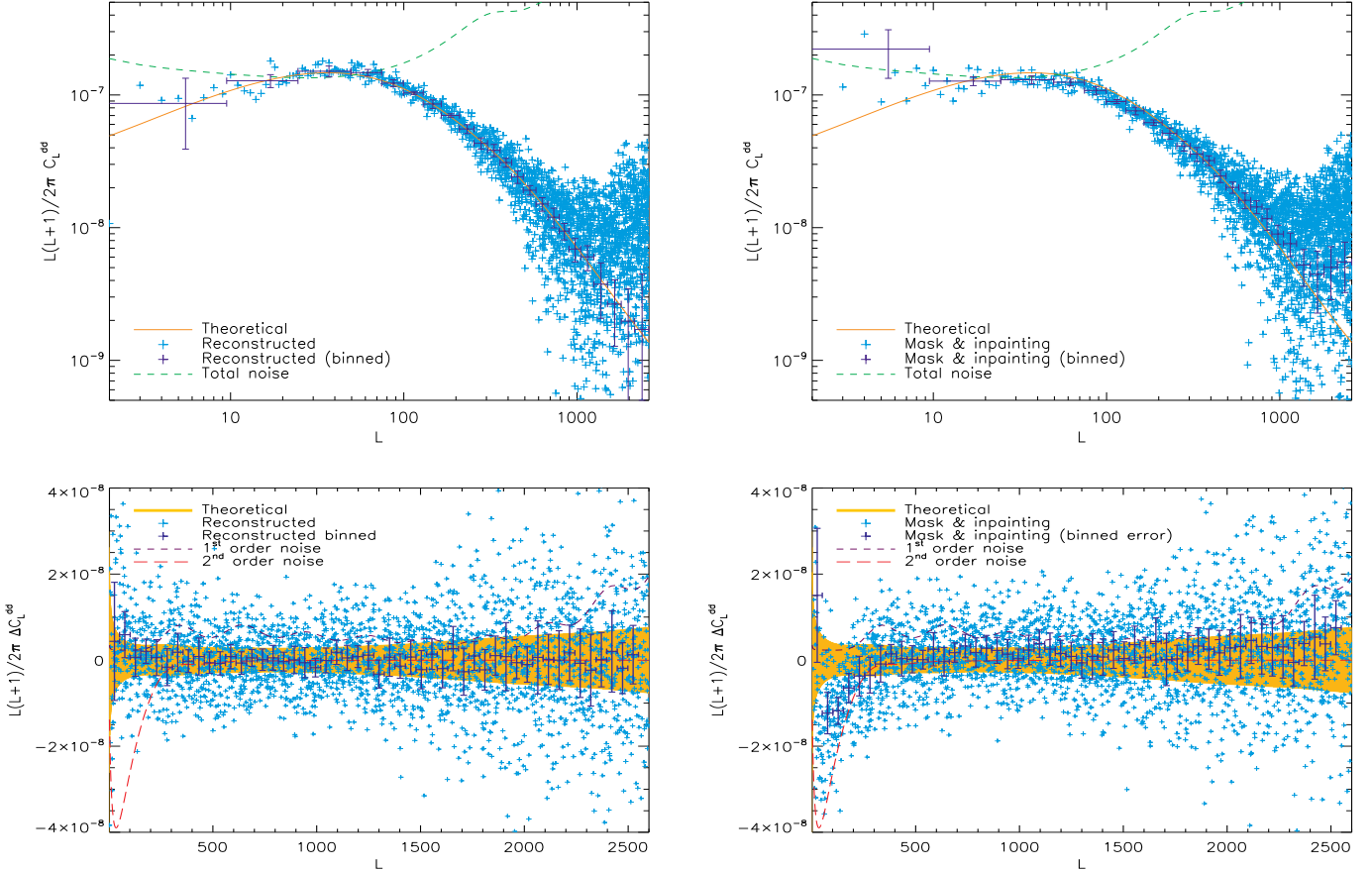


Fig. 6. Impact of the masking corrected by an *inpainting* process. The left panels are for the full-sky PLANCK synthetic lensed temperature maps whereas the right panels compile the results drawn from the masked lensed temperature maps restored with the *inpainting* process described in Sect. 4.4. *Upper panels:* the reconstructed deflection APS $\widehat{C}_L^{\text{dd}}$, obtained from the projected potential APS estimate of Eq. (28). The (light blue/grey) crosses show the $\widehat{C}_L^{\text{dd}}$ per multipole and the (dark blue/black) data points are the band-power $\widehat{C}_L^{\text{dd}}$. The horizontal intervals represent the averaging multipole bands and the vertical ones the 1σ error. The (orange solid) line figures the fiducial deflection angle APS C_L^{dd} and the (green dashed) line the total noise of the quadratic estimator ($N_L^{(0)} + N_L^{(1)} + N_L^{(2)}$). *Lower panels:* the bias of the deflection APS reconstruction ΔC_L^{dd} defined as the difference between the reconstructed deflection APS $\widehat{C}_L^{\text{dd}}$ and the input deflection APS C_L^{dd} . Consistently with the upper panels, (light blue/grey) crosses are ΔC_L^{dd} per multipole and (dark blue/black) data points are the band power ΔC_L^{dd} with the associated averaging multipole widths (horizontal intervals) and 1σ error (vertical intervals). The large (orange/grey) band shows the analytical $\pm 1\sigma$ errors per band power expected for the quadratic estimator (see Eq. 21). Finally, the lines show the non-Gaussian sub-dominant noise terms at the first-order (violet/dashed) and at the second-order (red/long dashed) in $C_L^{\phi\phi}$.

we further assume the set $\{d^j(\hat{n})\}$ forms an orthonormal basis. Recovering the missing pixel can then be made by for a solution that minimizes the sparsity of the $\mathcal{T}(\hat{n})$ in \mathcal{D} . As in 3.2, an appropriate sparsity estimate of $\mathcal{T}(\hat{n})$ in \mathcal{D} consists in measuring the sum of the absolute values of $\alpha_j = \langle \mathcal{T}(\hat{n}), d^j(\hat{n}) \rangle$. The recovered CMB map is then obtained by solving the following optimization problem :

$$\min_{\{\mathcal{T}(\hat{n})\}} \sum_j |\langle \mathcal{T}(\hat{n}), d^j(\hat{n}) \rangle| \text{ s.t. } \|\mathcal{T}(\hat{n}) - \mathcal{M}(\hat{n})T(\hat{n})\| < \epsilon \quad (30)$$

where ϵ stands for the reconstruction error. It has been shown in Abrial et al. (2008) that this inpainting technique leads to very good CMB recovery results. Our inpainting algorithm can be found in Abrial et al. (2007, 2008) and its implementation is based on the Multi-Resolution on the Sphere (MRS) package⁸.

⁸ <http://jstarck.free.fr/mrs.html>

In the following, we seek to assess the impact of the *inpainting* mask correction in PLANCK-like maps on a CMB lensing reconstruction.

4.5. Effect of inpainting

First, we have to choose a realistic mask, which could apply to the forthcoming PLANCK temperature map. However, depending on the details of the component separation pipeline the different methods developed in the PLANCK consortium (see Leach et al. 2008), yield to slightly different masks. Furthermore, the mask size is not a necessary criteria for the final choice of the component separation method that will be selected for the PLANCK data analysis. We thus adopt a conservative approach, which consists in choosing the union of the masks provided by each of the methods at the time of the Component Separation PLANCK *Working*

Group second challenge (Leach et al. 2008). Such a mask, hereafter referred to as the *union mask*, rejects about 11% of the sky, as shown in the Fig 5.

Then the 10 PLANCK-like lensed CMB temperature maps we have generated (see Sect. 4.2) are masked according to the *union mask* and then restored by applying the *inpainting* method described in Abrial et al. (2008). From each of these mask corrected maps, we extract a projected potential field using the quadratic estimator of Eq. (25). As previously, the results are compiled in the form of the average projected potential APS $\widehat{C}_L^{\phi\phi}$ following Eq. (28). The reconstructed deflection APS, given by $\widehat{C}_L^{\text{dd}} = L(L+1)\widehat{C}_L^{\phi\phi}$, as well as the bias between estimated and fiducial deflection APS ΔC_L^{dd} are shown in the right panels of Fig. 6.

We find that the mask corrected by the inpainting results in a marginal increase ($\sim 4\%$) of the 1σ errors on the estimated deflection APS (hence on the projected potential APS). Masking and inpainting causes an increase of the reconstructed APS bias ΔC_L^{dd} arising mostly at large angular scale corresponding to multipole $L < 300$. However, this bias is weaker than the sub-dominant second-order in $C_L^{\phi\phi}$ non-Gaussian bias. Fig. 6 shows a clear increase of power in the very first multipole band ($2 < l < 10$). In this multipole range, PLANCK is not expected to achieve a good reconstruction of the potential APS (Hu & Okamoto 2002). From the multipole $L = 300$ up to $L = 2600$, the bias stays below the first-order in $C_l^{\phi\phi}$ non-Gaussian bias and is compatible with the theoretical 1σ errors expected for the quadratic estimator. From fully controlling the inpainting impact, one might want to push further the study by analytically calculating or Monte-Carlo estimating the mask induced bias. However, it is not mandatory for reconstructing the projected potential APS with PLANCK. The masking effect, once corrected by inpainting, becomes a sub-dominant systematic effect that can be safely neglected.

4.6. Robustness against the unresolved point sources

Up to now, we have handled independently two important issues linked to the presence of foreground emissions in the observation maps, the impact of the foreground residuals after component separation with GMCA in Sect. 3.3 and the impact of the masking corrected with the inpainting method in the previous subsection (Sect. 4.5). We found that none of them compromises our ability to reconstruct the deflection APS. In a more realistic approach, these two issues should be handled altogether, as the inpainting process is intended to be applied on a CMB map contaminated by foreground residuals. The presence of foreground residuals is susceptible to harden the inpainting process and consequently degrade the CMB lensing recovery. Here, we assess the robustness of the deflection reconstruction on masked and inpainted CMB maps when adding infra-red point sources residuals. This choice is motivated for two reasons. The point sources residuals after component separation is a well-known matter of concern in any CMB non-gaussianities analysis and the emission of the infra-red sources population is one of the major foreground contaminant at the PLANCK-HFI observation channels.

We use the full-sky map of infra-red point sources residuals after a component separation using GMCA, we had estimated in Sect. 3.2. This point sources residuals is added to the 10 synthetic PLANCK lensed CMB temperature maps described in Sect. 4.2. Then we redo the same analysis than previously in Sect. 4.5: the *union mask* is applied to the maps, cutting out the brightest infra-red sources, which have been detected during

the Component Separation PLANCK *Working Group* second challenge (Leach et al. 2008). The 10 masked maps are restored using the *inpainting* method before being ingested in the full-sky quadratic estimator of the projected potential field. The results of the whole analysis are presented in the form of the average reconstructed deflection APS and bias, and shown in Fig. 7.

We find that the inpainting performances are only marginally degraded (at $\leq 1\sigma$ level) by the presence of point sources residuals within the CMB maps, and this degradation occurs mainly at the two multipole extremes. At the lower multipoles ($L < 30$), the APS deflection reconstruction suffers from a 1σ increase of the bias, whereas at the higher multipoles, only the error bars increase. We conclude that the inpainting method succeeds in keeping the statistical properties of the CMB map unchanged even in presence of highly non-Gaussian foreground residuals and it is a qualified method to handle the masking issue when seeking at a CMB lensing recovery. In addition, the results compiled in the Fig. 7 give the total impact of point sources on the deflection reconstruction, as they account for both the masking of the bright detected sources and the unresolved residuals. We report that point sources are responsible for a total 13% increase of the 1σ errors on the reconstructed APS deflection, mainly induced by the unresolved residuals. As a summary, the major nuisance of point sources is related to the masking of the bright ones, which tend to increase the bias on the reconstructed deflection APS, whereas the unresolved residuals results mainly in an increase of the errors on the deflection retrieval.

Conclusions

The High Frequency Instrument (HFI) of the PLANCK satellite, which has been launched on the 14th of May 2009, has the sensitivity and the angular resolution required to allow a *reconstruction* of the CMB lensing using the temperature anisotropies map alone. The pioneer works to put evidence of the CMB lensing within the WMAP data are not directly applicable or not well-optimized to the PLANCK data. First, one might want to take benefit of the efficient component separation algorithms developed for PLANCK before applying a CMB lensing estimator rather than to correct the lensing reconstruction from the bias due to the foreground emission afterward. Second, we need an efficient and manageable method to take into account the sky cutting within the 50 Mega-pixels maps provided by PLANCK. In addition, the CMB lensing is related to another burning thematic: characterizing the non-Gaussianities of the temperature anisotropies (primordial non-Gaussianities, cosmic string, etc.).

We have implemented both the flat-sky and the all-sky versions of the quadratic estimator of the projected potential field described in Hu (2001b); Okamoto & Hu (2003) to apply them on PLANCK synthetic temperature maps. First, within the flat-sky approximation, we have prepared a *demonstration model*, which consists in running GMCA, a component separation method described in Bobin et al. (2008), on PLANCK frequency channel synthetics maps, containing the lensed CMB temperature, the PLANCK nominal instrumental effects (modeled by a white Gaussian noise and a Gaussian beam) and the three dominant foreground emissions at the PLANCK-HFI observation frequencies, namely the SZ effect, the galactic dust and the infra-red point sources. We have performed a Monte-Carlo analysis to quantify the impact of the foreground residuals after the GMCA on the projected potential field and APS reconstructions. Then, we have moved on to the full-sky case, using the LensPix algorithm (Lewis 2005) to generate lensed CMB temperature maps at the PLANCK resolution. We have performed a Monte-Carlo anal-

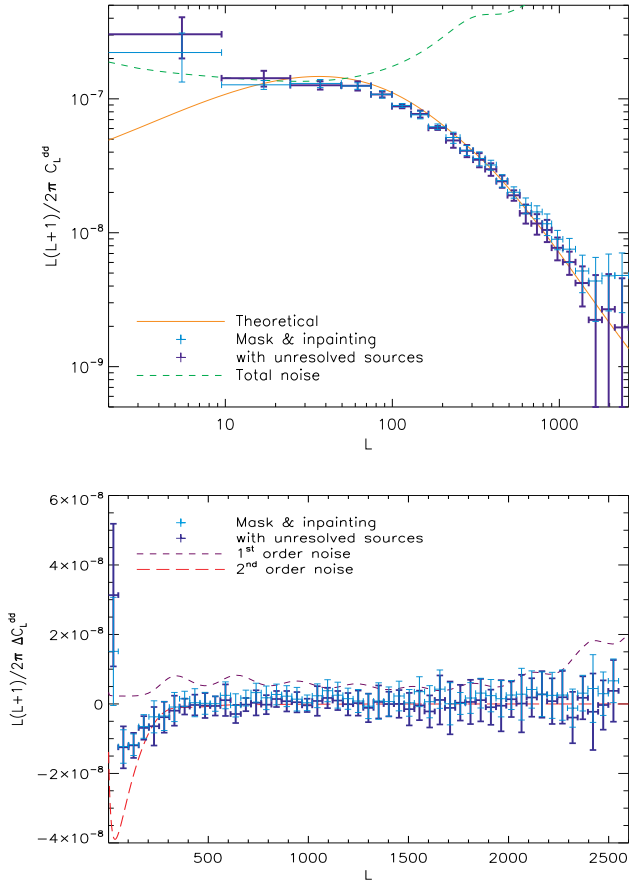


Fig. 7. Robustness of the inpainting to the unresolved point sources. The upper panel shows the reconstructed deflection APS whereas the lower panel the bias on the deflection APS reconstruction. The (dark blue/black) data points show the result of the full-sky quadratic estimation on the set of lensed CMB maps with point sources residuals, which have been masked then restored with the inpainting technique, as described in Sect. 4.6. For comparison, the results obtained in Sect. 4.5, in the case without any sources residuals, have been copied out on here as (light blue/grey) crosses. The fiducial analytical deflection APS as well as the total reconstruction noise and the two APS bias are shown following the same representation code as in Fig. 6, and horizontal and vertical intervals have the same meaning as described in the Fig. 6 caption. For a sake of readability, only the *band power* reconstructed APS and APS bias are represented, and the theoretical error bars by multipole bins are not shown.

ysis to tackle the masking issue; we have used the *inpainting* method described in Abrial et al. (2008) to restore the PLANCK synthetic temperature maps, masked according to a realistic cut out of 11% of the sky, accounting for the bright detected point sources. By applying the projected potential quadratic estimator on these restored maps, we have studied the impact of the inpainting of the mask on the PLANCK sensitivity to the projected potential APS. Finally, we have assessed the total impact of the point sources emission, in confronting the inpainting method to the unresolved point sources residuals.

Results

1. Within our flat-sky *demonstration model*, we found that the reconstruction of the projected potential field is still feasible after a component separation using GMCA. More quantitatively, the foreground residuals in the GMCA output CMB maps lead to a 10% increase of the 1σ errors on the projected potential APS reconstruction when applying the quadratic estimator. The GMCA process results in an increase of the dispersion of the projected potential APS reconstruction, but this dispersion remains within the theoretical 1σ errors at all angular scales but the $L < 60$ multipoles, in which the flat-sky analysis is expected to show some limitations anyway. Such a study dealing with the impact of a component separation process on the CMB lensing reconstruction had never been performed before. Our results allow us to assess that applying a component separation algorithm on the frequency channel CMB maps before any lensing estimation is a well-adapted strategy for the sake of the projected potential reconstruction within PLANCK.
2. For the full-sky reconstruction of the projected potential APS with PLANCK, we report that a realistic 11% of the sky mask, applied on some PLANCK-nominal lensed CMB temperature maps, has a negligible impact on the CMB lensing signal retrieval process, whenever it has been corrected by the *inpainting* method of Abrial et al. (2008) beforehand. More precisely, the bias on the estimated projected potential APS induced by the mask after inpainting is always either compatible with the theoretical 1σ errors (from $l = 300$ up to $l = 2600$) or weaker than the second-order in $C_l^{\phi\phi}$ non-Gaussian bias (in the $l < 300$ range). The major impact of the inpainting correction on the projected potential APS arises at the larger angular scales ($2 < l < 10$), which are not expected to be well-reconstructed with PLANCK. In addition, these results have not significantly changed after the introduction of unresolved point sources residuals. When treating the point sources emission in a comprehensive way, we report a 13% increase of the 1σ errors on the reconstructed deflection APS on average, resulting mainly from the unresolved point sources residuals, whereas the level of bias is marginally increased at low multipoles. We conclude that applying the inpainting method of Abrial et al. (2008) beforehand is a good strategy to take into account the masking issue when seeking at reconstructing the projected potential with PLANCK.

Perspectives Our results on the CMB lensing reconstruction are the first step to elaborate a complete analysis chain dedicated to the projected potential APS reconstruction with the PLANCK data. Such a CMB lensing reconstruction pipeline should involve a component separation and a bright point sources detection followed by an algorithm to correct from the mask (e.g. the inpainting method) before applying a quadratic estimator of the projected potential field on the resulting CMB temperature map.

We plan to go on developing in parallel both the flat-sky and the full-sky reconstruction tools. The flat-sky tools will allow us to perform a multi-patches CMB lensing reconstruction in cutting several hundred patches out of the most foreground cleaned region of the full-sky map. Using such a method requires a quantitative study of the impact of the sphere-to-plan projection and the sharp edge cuts effects beforehand. As a first task, we should test whether our results concerning the feasibility of reconstructing the CMB lensing after a component separation and after an inpainting of the mask still hold when dealing with the fully realistic PLANCK simulation (including e.g. non axisymmetric beam,

inhomogeneous noise and correlated foreground emissions). As long as we can demonstrate we have a sufficient control on systematics, we will be ready to measure the projected potential APS with PLANCK alone. Such an additional cosmological observable is expected to enlarge the investigation field accessible to the PLANCK mission from the primordial Universe to us.

Acknowledgements. We warmly thank Duncan Hanson for providing us the second-order non-Gaussian noise term biasing the projected potential APS estimation and for helpful discussions. We also would like to thank Martin Reinecke for his help on the HEALPix package use. We acknowledge use of the CAMB, LENSPix, HEALPix-Cxx and MRS packages. This work was partially supported by the French National Agency for Research (ANR-05-BLAN-0289-01 and ANR-08-EMER-009-01).

References

- Abrial, P., Moudden, Y., Starck, J., et al. 2007, *Journal of Fourier Analysis and Applications*, 13, 729
- Abrial, P., Moudden, Y., Starck, J.-L., et al. 2008, *Statistical Methodology*, 5, 289, arXiv:0804.1295
- Aghanim, N. & Forni, O. 1999, *A&A*, 347, 409
- Amblard, A., Vale, C., & White, M. 2004, *New Astronomy*, 9, 687
- Argüeso, F., González-Nuevo, J., & Toffolatti, L. 2003, *ApJ*, 598, 86
- Babich, D. & Pierpaoli, E. 2008, *ArXiv e-prints*, 803
- Barreiro, R. B., Martínez-González, E., Vielva, P., & Hobson, M. P. 2006, *MNRAS*, 368, 226
- Bernardeau, F. 1997, *A&A*, 324, 15
- Blanchard, A. & Schneider, J. 1987, *A&A*, 184, 1
- Bobin, J., Moudden, Y., Starck, J.-L., Fadili, J., & Aghanim, N. 2008, *Statistical Methodology*, 5, 307
- Challinor, A. & Lewis, A. 2005, *Phys. Rev. D*, 71, 103010
- Delabrouille, J., Cardoso, J.-F., & Patanchon, G. 2003, *MNRAS*, 346, 1089
- Delabrouille, J., Melin, J.-B., & Bartlett, J. G. 2002, in *ASP Conf. Ser. 257: AMiBA 2001: High-Z Clusters, Missing Baryons, and CMB Polarization*, 81
- Elad, M. and Starck, J.-L., Querre, P., & Donoho, D. 2005, *Applied and Computational Harmonic Analysis*, 19, 340
- Górski, K. M., Hivon, E., Banday, A. J., et al. 2005, *ApJ*, 622, 759
- Granato, G. L., De Zotti, G., Silva, L., Bressan, A., & Danese, L. 2004, *ApJ*, 600, 580
- Guzik, J., Seljak, U., & Zaldarriaga, M. 2000, *Phys. Rev. D*, 62, 043517
- Hanson, D., Challinor, A., Efstathiou, G., & Bielewicz, P. 2009, in preparation
- Hirata, C. M., Ho, S., Padmanabhan, N., Seljak, U., & Bahcall, N. 2008, *ArXiv e-prints*, 801
- Hirata, C. M. & Seljak, U. 2003a, *Phys. Rev. D*, 67, 043001
- Hirata, C. M. & Seljak, U. 2003b, *Phys. Rev. D*, 68, 083002
- Hu, W. 2000, *Phys. Rev. D*, 62, 043007
- Hu, W. 2001a, *Phys. Rev. D*, 64, 083005
- Hu, W. 2001b, *ApJ*, 557, L79
- Hu, W. 2002, *Phys. Rev. D*, 65, 023003
- Hu, W. & Okamoto, T. 2002, *ApJ*, 574, 566
- Kamionkowski, M., Kosowsky, A., & Stebbins, A. 1997, *Physical Review Letters*, 78, 2058
- Kaplinghat, M., Knox, L., & Song, Y.-S. 2003, *Physical Review Letters*, 91, 241301
- Kesden, M., Cooray, A., & Kamionkowski, M. 2003, *Phys. Rev. D*, 67, 123507
- Knox, L. & Song, Y.-S. 2002, *Physical Review Letters*, 89, 011303
- Komatsu, E. 2002, *ArXiv Astrophysics e-prints*
- Leach, S. M., Cardoso, J., Baccigalupi, C., et al. 2008, *ArXiv e-prints*, 805
- Lesgourgues, J., Perotto, L., Pastor, S., & Piat, M. 2006, *Phys. Rev. D*, 73, 045021
- Lewis, A. 2005, *Phys. Rev. D*, 71, 083008
- Lewis, A. & Challinor, A. 2006, *Phys. Rep.*, 429, 1
- Lewis, A., Challinor, A., & Lasenby, A. 2000, *Astrophys. J.*, 538, 473
- Masnou, S. & Morel, J.-M. 1998, in *ICIP*, ed. IEEE, Vol. 3, 259–263
- Okamoto, T. & Hu, W. 2003, *Phys. Rev. D*, 67, 083002
- Park, S. K. & Schowengerdt, R. A. 1983, *Computer Graphics Image Processing*, 23, 258
- Perotto, L., Lesgourgues, J., Hannestad, S., Tu, H., & Y Y Wong, Y. 2006, *Journal of Cosmology and Astro-Particle Physics*, 10, 13
- Riquelme, M. A. & Spergel, D. N. 2007, *ApJ*, 661, 672
- Seljak, U. & Hirata, C. M. 2004, *Phys. Rev. D*, 69, 043005
- Seljak, U. & Zaldarriaga, M. 1997, *Physical Review Letters*, 78, 2054
- Serjeant, S. & Harrison, D. 2005, *MNRAS*, 356, 192
- Smith, K. M., Zahn, O., & Doré, O. 2007, *Phys. Rev. D*, 76, 043510
- Su, M. & Yadav, A. P. S. and Zaldarriaga, M. 2009, arXiv:0901.0285v1
- Sunyaev, R. A. & Zeldovich, Y. B. 1970, *Comments on Astrophysics and Space Physics*, 2, 66
- Takada, M. & Futamase, T. 2001, *ApJ*, 546, 620
- Tauber, J. A. 2006, in *The Many Scales in the Universe: JENAM 2004 Astrophysics Reviews*, ed. J. C. Del Toro Iniesta, E. J. Alfaro, J. G. Gorgas, E. Salvador-Sole, & H. Butcher, 35–+
- The Planck Consortia. 2005, *Planck: the scientific programme*, Vol. ESA-SCI(2006)1 (European Space Agency), available at arXiv:astro-ph/0604069
- Zaldarriaga, M. 2000, *Phys. Rev. D*, 62, 063510
- Zaldarriaga, M. & Seljak, U. 1998, *Phys. Rev. D*, 58, 023003